



Article

# Wind Effects on Dome Structures and Evaluation of CFD Simulations through Wind Tunnel Testing

Tiantian Li <sup>1</sup>, Hongya Qu <sup>2</sup>, Yi Zhao <sup>3</sup>, Ryan Honerkamp <sup>3</sup>, Guirong Yan <sup>3,\*</sup>, Arindam Chowdhury <sup>4</sup> and Ioannis Zisis <sup>4</sup>

- <sup>1</sup> Shanghai Typhoon Institute of China Meteorological Administration, Shanghai 200030, China
- <sup>2</sup> Department of Bridge Engineering, Tongji University, Shanghai 200092, China
- Department of Civil, Architectural and Environmental Engineering, Missouri University of Science and Technology, Rolla, MO 65409, USA
- Department of Civil and Environmental Engineering, Florida International University, Miami, FL 33174, USA
- \* Correspondence: yang@mst.edu

Abstract: In the study, a series of wind tunnel tests were conducted to investigate wind effects acting on dome structures (1/60 scale) induced by straight-line winds at a Reynolds number in the order of 106. Computational Fluid Dynamics (CFD) simulations were performed as well, including a Large Eddy Simulation (LES) and Reynolds-Averaged Navier-Stokes (RANS) simulation, and their performances were validated by a comparison with the wind tunnel testing data. It is concluded that wind loads generally increase with upstream wind velocities, and they are reduced over suburban terrain due to ground friction. The maximum positive pressure normally occurs near the base of the dome on the windward side caused by the stagnation area and divergence of streamlines. The minimum suction pressure occurs at the apex of the dome because of the blockage of the dome and convergence of streamlines. Suction force is the most significant among all wind loads, and special attention should be paid to the roof design for proper wind resistance. Numerical simulations also indicate that LES results match better with the wind tunnel testing in terms of the distribution pattern of the mean pressure coefficient on the dome surface and total suction force. The mean and root-mean-square errors of the meridian pressure coefficient associated with the LES are about 60% less than those associated with RANS results, and the error of suction force is about 40-70% less. Moreover, the LES is more accurate in predicting the location of boundary layer separation and reproducing the complex flow field behind the dome, and is superior in simulating vortex structures around the dome to further understand the unsteadiness and dynamics in the flow field.

**Keywords:** wind loads; Computational Fluid Dynamics simulation; wind tunnel testing; spherical domes; turbulence modeling



Citation: Li, T.; Qu, H.; Zhao, Y.; Honerkamp, R.; Yan, G.; Chowdhury, A.; Zisis, I. Wind Effects on Dome Structures and Evaluation of CFD Simulations throughWind Tunnel Testing. Sustainability 2023, 15, 4635. https://doi.org/10.3390/ su15054635

Academic Editors: Junsheng Su, Xiaohui Yu, Yutao Pang and Xiyin Zhang

Received: 24 January 2023 Revised: 24 February 2023 Accepted: 2 March 2023 Published: 5 March 2023



Copyright: © 2023 by the authors. Licensee MDPI, Basel, Switzerland. This article is an open access article distributed under the terms and conditions of the Creative Commons Attribution (CC BY) license (https://creativecommons.org/licenses/by/4.0/).

#### 1. Introduction

Spherical domes are commonly used as long-span space structures for public assembly venues, such as conference centers, concert halls, arenas, etc., since such a structure is at a distinct advantage due to high space usage and economic benefits. An example of a spherical building shown in Figure 1 is the Avicii Arena in Stockholm, Sweden. Its diameter is 110 m, and its inner height is 85 m. Winds can generate large loads on dome structures because of their large outer surface area, as well as severe vibrations because of their long-span and lightweight roofs. In fact, dome structures have suffered significant damage, and even total collapse, during past strong wind events. For example, the New Orleans Superdome suffered severe damage including the loss of its roof during Hurricane Katrina in 2005 (Figure 2a). The Reno/Virginia peak dome collapsed due to strong wind gusts in Western Nevada in 2008 (Figure 2b). Therefore, the wind resistance design of dome structures for structural failure elimination and safety assurance is necessary, and the aerodynamic behavior of dome structures and wind-induced loads need to be well understood.

Sustainability, **2023**, 15, 4635 2 8f 23

Sustainability 2023, 15, 4635

dome structures for structural failure elimination and safety assurance is necessary, and the aerodynamic behavior of dome structures and wind-induced loads need to be well understood:



Figure 1: Avisii Arena in Stockholm, Sweden (by Stockholm Live):

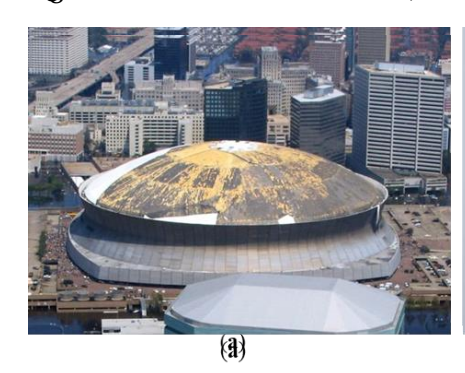




Figure 2: (a) The New Orleans Superdome badly damaged during Hurricane Katrina (by Trahan Architects/Asm Global); (b) The Reno/Virginia peak dome collapsed due to strong wind gusting (by NWS Reno, Nevada).

Wind tunnel tests were first conducted to explore mean [12] and fluctuating [3,4] wind pressures acting on dome structures. The impact of the Reynolds main [4,2] and fluctuating [3,4] pressures acting on dome structures. The impact of the Reynolds humber [4,7] of spacetimes are acting on dome structures. The impact of the Reynolds humber [4,7] of spacetimes with pressure at the dome structures are impact of the Reynolds humber [4,7] of spacetimes are supported by the dome spacetimes with increasing the interpretation of the pressure at the dome spacetime and the decreased, and [2]. However, moders the pressure at the dome spacetime appearing the pressure at the dome spacetime appearing the pressure at the dome spacetime appearing the pressure at the dome spacetime and the dome spacetime appearing the pressure at the dome spacetime and the dome spacetime at the dome spacetime at the dome spacetime at the dome spacetime at the dome spacetime and the dome spacetime at the dome spacetime THE HOLD THE WAS LESS OF THE PROPERTY OF THE P 53 × 104 100 2.9 × 108 and concluded that the chressure distribution becames Records pendent when it tall within 1.12-2.20 & 1.05 121. As polypospic londs and semi-air solutions. inder under various aust trequencies ware studied apata theoratical model was proposed to his exparimental results is a Windstung litests of nome structures with various height toespane ration and concing cration were renducted the inventigate wind threselves on he tractable dame roots [9,10] Mean pressure coefficients increased with the increase of the height-to-span ratio. Additionally, as the opening ratio increased suction pressure coefficients, at the routinest interior at open dome roots, increased, a certes he measurements twere carried out for an array of three domes, and the peak suction was observed approximately at the apex of the first dome and the maximum positive pressure was observed Butthe Windward side of the third done with he provide more details to understand flow characomputational Third Dynamics (CFD) cimulations are also employed to study catery disparaticide havious of element structures ownich provide more details to understande flow wheracteristics regarding boundary daver separation of this how save governed by the well-known haviet-stakes (A+S) conations which describe every detail as the turbulent slow field from the largest of the smallest length and time scales. Three types of incurrences (RANS) simulation. The DNS directly solves N-S equations and resolves all scales of motion, and therefore, fine grid resolution down to the Kolmogorov scale is required. For example, the total number of grid points is estimated to be 10<sup>13</sup> for a three-dimensional simulation of a turbulent flow with a Reynolds number of 10<sup>6</sup> [12]. Due to the high

Sustainability **2023**, 15, 4635 3 of 22

computational demand of the DNS, its application to wind engineering is difficult and limited, especially for high Reynolds number problems. To reduce computational demand, the LES is developed to only resolve large scales of motion while smaller scales are removed from the flow variables by filtering the original N–S equations in the physical space. Smaller scales are then analyzed by subgrid-scale models, such as the Smagorinsky–Lily model [13], the wall-adapting local eddy-viscosity (WALE) model [14], and the dynamic Smagorinsky–Lilly model [15,16].

In the RANS simulation, N-S equations are averaged over all scales of motion, and therefore, the turbulent flow is described by statistical parameters, e.g., mean velocity. The effects of turbulent fluctuations on the averaged flow are represented by additional terms obtained in the averaging process, which are called Reynolds stresses prescribed by turbulence models. Turbulence models are categorized according to the number of required transport equations. For a one-equation model, there is only one transport equation, and the Spalart–Allmaras (SA) model [17] is commonly used. The SA model shows the reasonably robust and time efficient capability to solve mildly separated flows. Additionally, it uses less memory and converges easily. For the two-equation model, there are two transport equations. The standard  $k-\varepsilon$  [18] and standard  $k-\omega$  models [19] are commonly deployed. Turbulent kinetic energy is described by k, and the dissipation rate of k is described by  $\varepsilon$ and  $\omega$ . Due to the fact that k at the impinging region is overestimated by the standard k- $\varepsilon$ model when the airflow passes over an isolated obstacle [12], the realizable k- $\varepsilon$  model [20] and renormalization group (RNG) k- $\epsilon$  model [21] are developed. The standard k- $\omega$  model is sensitive to inlet boundary conditions, and then the shear stress transport (SST)  $\emph{k-}\omega$ model [22–24] is developed, which predicts boundary layer separation and reattachment more accurately.

The LES and RANS simulations with the RNG k- $\varepsilon$  turbulence model were applied to study velocity profiles in the wake of a dome [25,26]. The RNG k- $\varepsilon$  model performed worse in simulating flow characteristics in the wake of the dome, and the LES showed better agreement with measurements. The LES was also applied to simulate mean pressures acting on a dome structure, which matched fairly well with experimental results [27]. Locations of boundary layer separation were predicted through the LES utilizing different subgrid-scale models, consisting of the Smagorinsky-Lily model, the WALE model, and the dynamic Smagorinsky-Lily model [28]. Since very fine grids were used in the LES, only minor deviations among different subgrid-scale models were observed. Wind pressures on scallop domes with a parabolic form of grooving were studied based on CFD simulations, and equations for surface pressure distribution were developed considering different height-tospan ratios [29]. Intensive CFD studies were conducted for dome structures to explain the capability of the CFD technique for determining appropriate design wind data [30]. It was concluded that pressure coefficients on the windward side and apex of the dome agreed well with corresponding Euro Code values, while pressure coefficients on the leeward side were different from all code standards. Wind loads acting on fifteen traditional domes were simulated by the CFD approach, and wind loads, especially suction force, were significantly affected by the shape of the dome [31].

The literature reviewed indicates that the DNS is able to provide every detail of the turbulent flow, but it is difficult to implement in flows of practical interest because of high computational demand. In comparison to the RANS simulation, the main properties of turbulent flows can generally be obtained by the LES with higher accuracy, but at a cost of higher memory usage and CPU time [32–34]. The accurate calculation of turbulent flow properties affects the reproduction of the flow structure of the wind field and hence, the accuracy of the wind pressure distribution on the dome surface. Considering respective advantages of the LES and RANS simulations, both of them are adopted in the current study. In the RANS simulation, the SA and SST k- $\omega$  turbulence models are selected because better prediction of boundary layer separation and reattachment can be achieved. Moreover, they can obtain relatively accurate results while reserving computational efficiency and good convergence. The LES is also employed because it is time-dependent and can

accuracy of the wind pressure distribution on the dome surface. Considering respective advantages of the LES and RANS simulations, both of them are adopted in the current study. In the RANS simulation, the SA and SST  $k-\omega$  turbulence models are selected because better prediction of boundary layer separation and reattachment can be achieved. Moreover, they can obtain relatively accurate results while reserving computational effective for the second secon ciency and good convergence. The LES is also employed because it is time-dependent and can reproduce turbulence with much higher accuracy. For wind engineering applications, reproduced upbrilence with much higher of the TOPD Formwint deriginesting application by the ingrimoniplactive to accurace on of too that CFDs in wintign results distribution not treating to salidate Theirescrutary winder pradictioning windspressure distribution on the edomect unface. Nistratorar the razinal tempolitective referencement trueture are first powerine wind texbist Natural Flazzird surgivering Resental Linerastinetary (NHERR) Will pawing a resental Enviety AVA Wherhatrel evide Interestioned Noiverette FILM and the mit was composed use papercharaction valuate, the BANS and LETS sinculations eTheotrescurrent their nexistas follows: seits, the dome escentu, experiment for the series of the experimental returns inouting and seared sexpensioners at results are analyzed and discussed the hirds the hebitesed RANS simulations are applied to authorically cimulate, the wind tunnel testing, and then their performances are evaluated. Finally, conclusions are drawn.

This section consists of four parts. First, the geometry of the dome structure is de-This section consists of four parts. First, the geometry of the dome structure is de-scribed. Then, the WOW EF at FIU is briefly introduced. The experimental setup in the scribed. Then, the WOW EF at FIU is briefly introduced. The experimental setup in the WOW EF is then followed. Finally, all testing cases are explained.

#### 2.1. Donne Geometry

The apex height and based inneter of the prototopy do mentructure are alemond 120 120 respectively. And all deplease 160 in selected and therefore, the selected name model has an apex height of  $H \equiv 0.67$  m and a base diameter of  $D \equiv 2.0$  m (Figure 3). The dome model is constructed with a smooth shell whose thickness is 9.0 mm. The blockage ratio, which is defined as the ratio of the projected area of the dome model and the test section of the WOW EF, is 0.7%. It is worth mentioning that the model scale of current testing is relatively large compared of provious actual for tox another bloc blash discussors a festbal testads domest from to their atendies are dies are maded y ham altern that 11 Such [1:5]-scukh wing a coale windy unad toping on the correspondence included in the ting results pnessarealiprobation distribution to type spracture estructure.

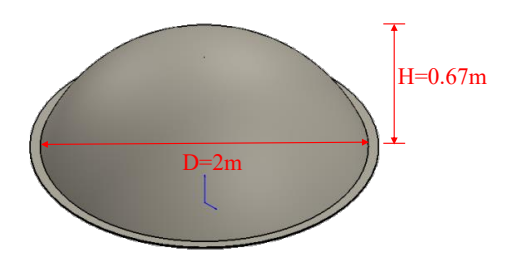


Figure 3: The dome model for wind tunnel testing:

2.2. Introduction of WOW EF
2.2. Introduction of WOW EF
Eigure 4 presents the WOW EF, which is a large wind tunnel with an open test section.
As shown in Figure 4a, it is housed in a 30.5 m × 24.4 m × 10.7 m building with a gate of the world in a 30.5 m × 24.4 m × 10.7 m building with a 30.5 m which we would not a 30.5 m tiona4As shown in Figure davie is housed in a 30 flow & 2,4 A crup 10.7 caregulding with speeds of 75.24 my s 2a14 be gevierated by weinterating is tallowed, and un to Cantegorie 5 to in displaced a ef. 702 m/fricae har generated by twelve faerate the Southern da Armall, singlat story building can be sufficiently aim to easier. The generated wind tield and thus small abundy see can be bestern at 14.25 cale regardence, the sixthey be avoid through the element and it your speet, on athilverarge28 on (Tisyra46), consisting of floor toughness, elements and for spirawty archieventarrante to boundaria lescricherente ristismentalier whose cui Andictors ce of 6. The access wall, which is used to stop wind-borne debris, is located 60 m to the North of the turning table center (Figure 4b).

turning table center (Figure 4b). from the flow conditioning section is the turning table, whose diameter is 4.9 m. The de-

5 of 22

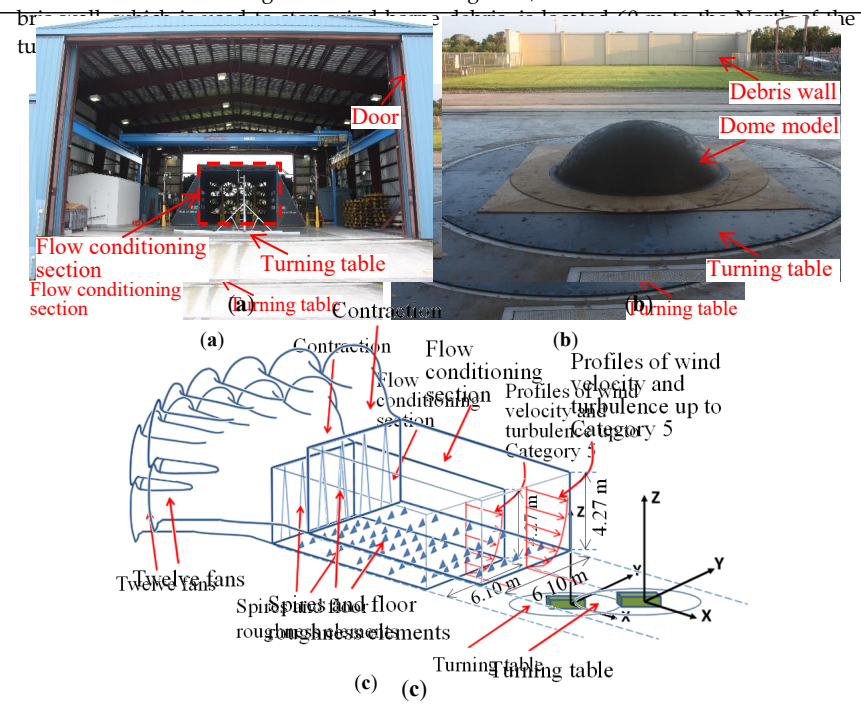
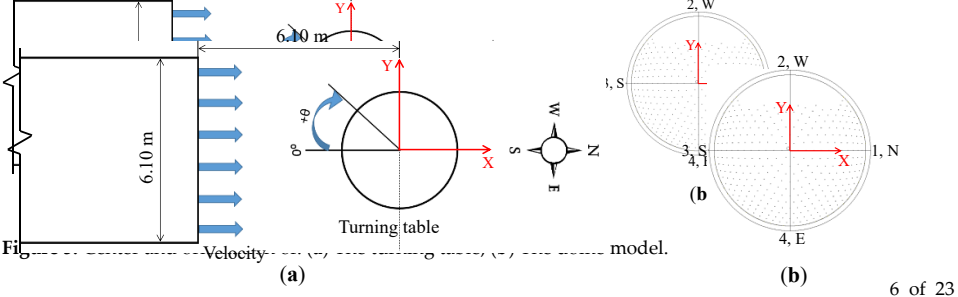


Figure 4. MoWiPW. E. v.a.) Flow management system and test section; (b) The model placed on top figure 4. The WOW EF: (a) Flow management system and test section; (b) The model placed on top of the turning table; (c) Schematic diagrams of the turning table; (c) Schematic diagrams of the WEP. WEF.

23. Experimentary setup
24. Experimentary setup
24. Experimentary setup
25. Experimentary setup
26. Ex



Sustainability **2023**, 15, 4635

Figure 5. Center and orientation of: (a) The turning table; (b) The dome model. Figure 5. Center and orientation of: (a) The turning table; (b) The dome model.



Figure 6. (a) Oppen terrain configuration with spires (b) Suburban terrain configuration with both spires and swifece counglesses alements.

The Cobra Probe manufactured by Turbulent Flow Instrumentation is used to measure the flow field at a frequency of 2500 Hz. It is a four-hole pressure probe, and resolves three components of velocity and local static pressure in real-time. The local coordinate system of the Cobra Probe is illustrated in Figure 7, which is used to calculate velocity components of each probe.

. .



Une now neigrating in the problem of the problem of

The Cobra Probe manufactured by Turbulent Flow Instrumentation is used to measure the flow field at a frequency of 2500 Hz. It is a four-hole pressure probe, and resolves three components of velocity and local static pressure in real-time. The local coordinate system of the Cobra Probe is illustrated in Figure 7, which is used to calculate velocity components of each probe.

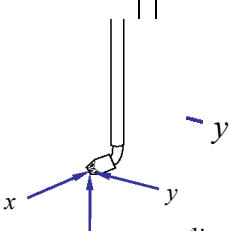


Figure 7. The coordinate system of the Cobra Physical Act different heights of 16.5 cm., 33.3 cm., 66.7 cm., and The Cobra Probes are installed at different heights of 16.5 cm., 33.3 cm., 66.7 cm., and 1.3.3 the Cobra Probes are installed at different heights of 16.5 cm., 33.3 cm., 66.7 cm., and 1.3.3 the Cobra Physical Control of the

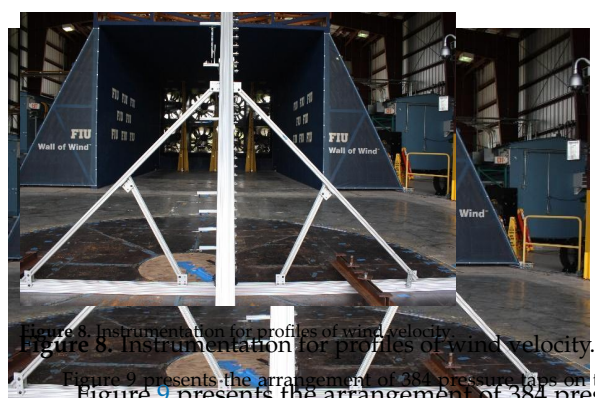


Figure 9 presents the arrangement of 38 pressure taps on the dome model, which are used to measure the strategy of the dome model, which are used to measure the strategy of the dome model, which are used to measure the strategy of the dome model and region in the positive strategy of the dome model and region in the positive Figure 8 that is not to be a considerable with the proof of the dome model. The taps of Scanivalve 20C33

electronic pressure scanners are deployed for data collection at frequencies of 520 Hz. An amolist up of pleasests of section of section at frequencies of 520 Hz. An amolist up of pleasests of section of secti

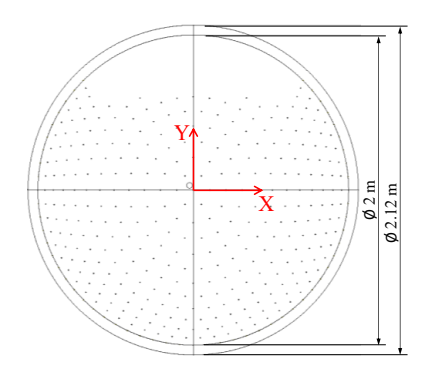


Figure 9. Presstre tipstalled anthe domine dome model.

#### 2.4. Testing Cases

Three different cases for the wind tunnel testing were conducted (Table 1). In Case 1, open terrain configuration is considered for the wind field and the dome is removed. In Cases 2–3, the dome is placed in the wind tunnel. The open terrain is employed in Case 2, while the suburban terrain is employed in Case 3. Within each case, three different levels of velocity are generated, i.e., 24 m/s (Level I), 34 m/s (Level II), and 44 m/s (Level III) at the height of 0.167 m (corresponding to 10 m in full scale).

Sustainability 2023, 15, 4635

Three different cases for the wind tunnel testing were conducted (Table 1). In Case 1, open terrain configuration is considered for the wind field and the dome is removed. In Cases 2–3, the dome is placed in the wind tunnel. The open terrain is employed in Case 2, while the suburban terrain is employed in Case 3. Within each case, three different levels of velocity are generated, i.e., 24 m/s (Level I), 34 m/s (Level II), and 44 m/s (Level III) at the height of 0.167 m (corresponding to 10 m in full scale).

Table 1. Cases for the wind tunnel testing.

	Case 1			Case 2			Case 3		
Dome model present?	No			Yes			Yes		
Terrain configuration	Open			Open			Suburban		
Wind speed level	I	ÎI	III	I	ĪI	III	I	II	III

#### 3. Experimental Results and Discussion

#### 3.1. Mean Velocity Profile

Profiles of mean wind velocity measured over the open terrain without the dome (Case 1) are depicted in Figure 10. Three different levels of velocity are generated, which are specified by the wind speed at the height of 0.167 m, 24 m/s (Level I), 34 m/s (Level II), and 44 m/s (Level III). To reduce measurement uncertainties, the first and last 10 s of each velocity time history are removed, and then the mean wind velocity is determined based on the middle range of the record. As the elevation increases, the mean velocity increases. The power law is used to fit mean velocity profiles, and the applied exponent is 9.5 for the Open terrain (Surface Roughness C) based on ASCE 7–16 [35]. The coefficients of determination ( $R^2$ ) of the power law fit for velocity Level I, Level II, and Level III are 0.75, 0.88, and 0.91, respectively. The mean velocity profile at Level III agrees with the power law the best.

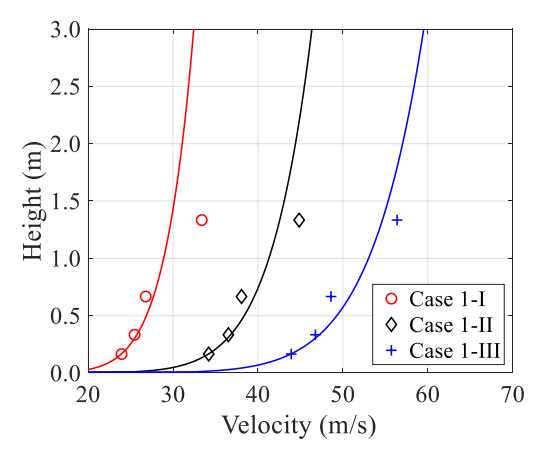


Figure 100. Problemes premedentativing what itselective for the robert pier with part the identification (Case 1).

3.2. Turbulence Intensity and Integral Length Scale

3.2. Turbulence Intensity and Integral Length Scale in Turbulence of the airflow is characterized by a scale expressed as a percentage, that is, turbulence of the airflow defined as their zedi by far so the expressed of sthep bucentage, twiting which expresses the intensity of the intensity of the intensity of the intensity of the mean velocity, according to the measured velocity time series (Equation (1)).

$$u' = \sqrt{\frac{1}{3}(u_X'^2 + u_Y'^2 + u_Z'^2)}$$

$$U = \sqrt{U_X^2 + U_Y^2 + U_Z^2}$$

$$u' = \sqrt{\frac{1}{3}(u_X'^2 + u_Y'^2 + u_Z'^2)}$$

$$U = \sqrt{U_X^2 + U_Y^2 + U_Z^2}$$

$$U = \sqrt{U_X^2 + U_Y^2 + U_Z^2}$$
(1)

Sustainability 2023, 15, 4635

ς

$$U = \int U_X^2 + U_Y^2 + U_Z^2$$
 8 of 22

where u' is the root-mean-square of the fluctuating components of the measured velo ityhele is istramoanneinesqueleccitythevieucthetiagnertipneeperioidhelmeesueldcielocitynponen dieistibicated by inclusive origins of each period in the theory of the original period in tindiante, das eubscript quartion of Z. Finar of Istherwith a Clobase as when the concentring in eight. I based on Equation (1). The TI slightly decreases with the increasing height. In general, they are all around 10% at different heights.

are all around 10% at different heights.

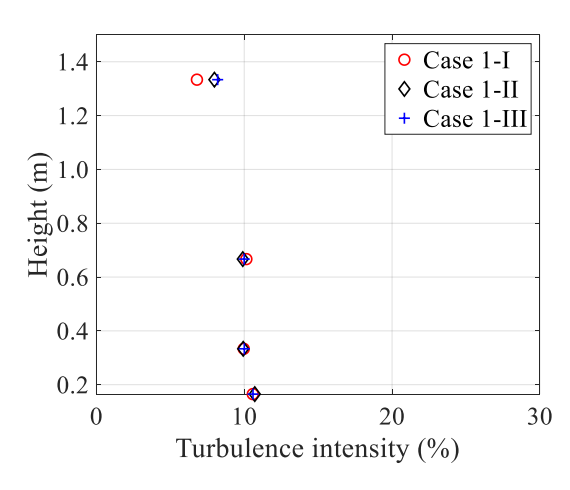


Figure 11. Trubulcher contente in the interior in the part of the part

The integral length scale of turbulence is a measure of the average size of turbulent eddiesh Thetestal densthase length walls reprise amegante of the average as it of the saverage as a construction of the saverage as a construc edstien Etheren saetotal infaniae, lengthe sealand representing three stirmentions and the eddic asslocityte the With the chemping it to divid a deterative verses gending text thinks in a position test dyst the test uctuation

where  $R(\tau)$  is the autocovariance function of the longitudinal velocity fluctuations. where  $R(\tau)$  is the autocovariance function of the longitudinal velocity fluctuations.

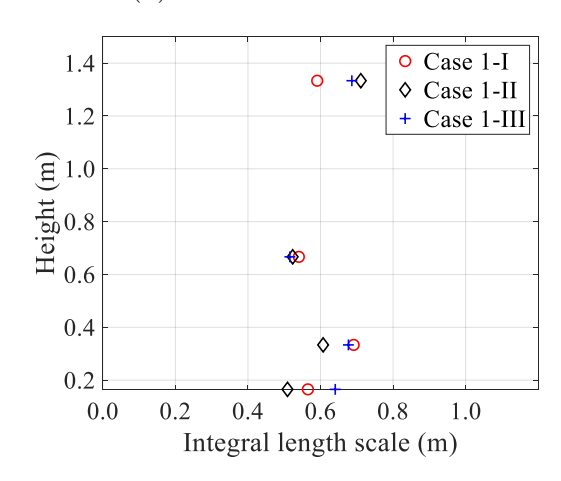


Figure 12. Integral de noting transcallen al beight engare poverter pein (Carrail). (Case 1).

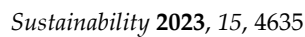
3.3. Power Spectral Density

 $10^{-2}$ 

3.3. Prover Spectral Density Presents the power spectral density (PSD) of velocity in the along-wind directinguate at Beignes on to 6then provincer superot fait cleans it y II (BSD) that experior city rain. the valong-w ancestical RED neightfoir b. 67 thy it the ESPEX) storcture extended an indicate the matter than the m the experimental data are higher ured FSDU spectrum, except at around 10 Hz where experimental data are higher.

Wind tunnel testing

--ESDU



#### 3.3. Power Spectral Density

Figure 13 presents the power spectral density (PSD) of velocity in the along-wind direction at a height of 0.67 m (dome apex) for Case 1-III over the open terrain. The measured PSD agrees fairly well with the ESDU spectrum, except at around 10 Hz where the experimental data are higher.

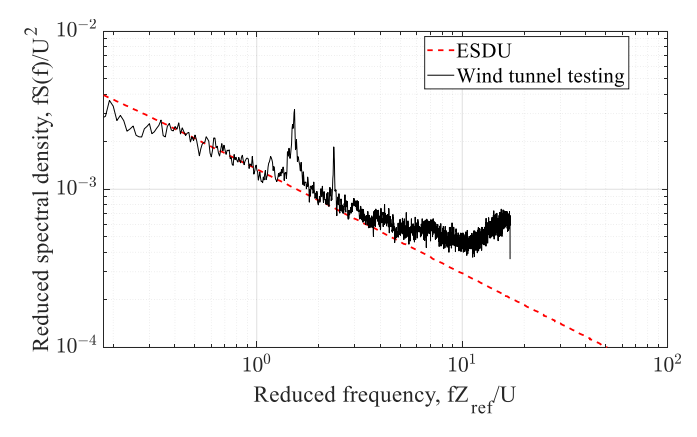


**Figure 13.** Power spectral density (PSD) of velocity in the along-wind direction at a height of 0.67 m (dome apex) over open terrain (Case 1-III).

#### 3:4: Reynolds Number

The Reynolds number is the ratio of inertial to viscous forces, which is defined as

$$ReRe = \frac{\rho V_0 V_1 H}{\mu \mu}$$
 (3)

where \$\text{p.s.} in the density of the kg/s/m\, and it is determined beard on the temperature two-CP, hambury density and and apprent pressure you kell as a unterprent the temperature of the step in the largest of the density at \$H\$ (27 m/s, 38 m/s, and 49 m/s from Case-10 ver the open terrain for respective velocity at \$H\$ (27 m/s, 38 m/s, and 49 m/s from Case-10 ver the open terrain for respective velocity levely; \$\text{\mu}\$ is dynamic viscosity of air when the aritemperature is 30°C (1.6686 \text{\mu} 1055 N is/m²). Based on Equation (3), the Reynolds numbers for three levels of velocity in Case 1 without the dome model are determined as 1.13 \times 100 (1.590 \times 100 msh 2.2505 10°100 present velocity.

#### 3.5. Mean Pressure Coefficient on the Center Meridian of the Model

The dimensionless number, the pressure coefficient ( $C_P$ ), is used to describe the relative wind pressure acting on the dome model. It is normalized by the dynamic pressure at the apex of the dome as:

$$C_{P_i} = \frac{P_i - P_{ref}}{\frac{1}{2}\rho V^2} \tag{4}$$

where  $P_i - P_{ref}$  is measured by the Scanivalve instrumentation, indicating the pressure difference between the local and reference pressure  $P_{ref}$ ; V is the reference mean velocity, which is the same as in Equation (3). In cases 2–3, the V from each wind speed level is used to calculate the pressure coefficient under the associated case, i.e., 27 m/s is used for wind speed level II, 38 m/s for wind speed level III.

Mean pressure coefficients ( $C_P$ ) on the center meridian of the dome model are presented in Figure 14. For all Cases, the profiles are of a similar shape, which are consistent with other reported studies [1,2,5,7]. The maximum pressure occurs at an elevation of about 20 degrees, and the minimum pressure appears at around 90 degrees. At around 45 degrees, the positive pressure changes to negative pressure. In addition, the pressure coefficient generally increases with inflow wind velocity, and the magnitude of the pressure coefficient over the suburban terrain is lower than that over the open terrain.

The results associated with Case 2-III are further compared to other studies with similar Reynolds numbers using smooth hemispheres in boundary layer flows [1,7]. Figure 15 indicates that the general trends among different studies are similar. A minor difference is found regarding the peak values of positive and negative pressure. At around 120 degrees, the curve of the present study is relatively different from the other two studies, implying that the pressure distribution on the leeward side of the dome may be different. This is

Sustainability 2023, 15, 4635

coefficient over the suburban terrain is lower than that over the open terrain.

The results associated with Case 2-III are further compared to other studies with similar Reynolds numbers using smooth hemispheres in boundary layer flows [1,7]. Figure 15 indicates that the general trends among different studies are similar. A minor difference is found regarding the peak values of positive and negative pressure. At around 120 de22 grees, the curve of the present study is relatively different from the other two studies, implying that the pressure distribution on the leeward side of the dome may be different. This is not allowed the different ratios of the model height to the diameter, which is 0.335 in the inches resent study and is 0 in for the other two studies.

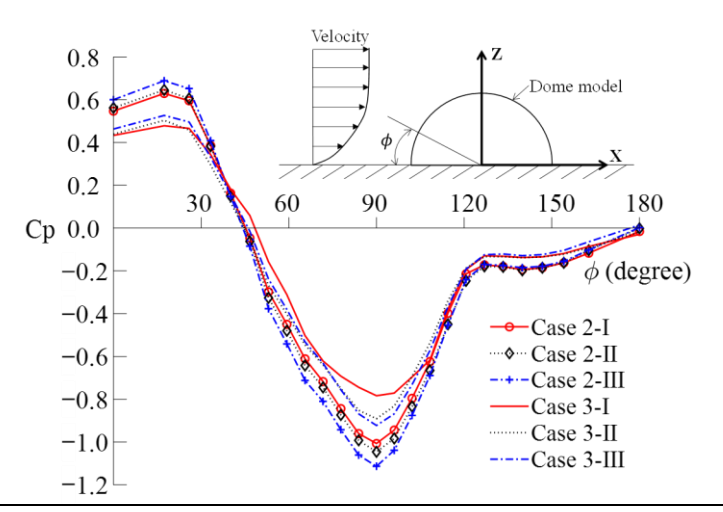


**Figure 14.** Comparison of pressure coefficient ( $C_P$ ) on the center meridian of the dome model.

11 of 23

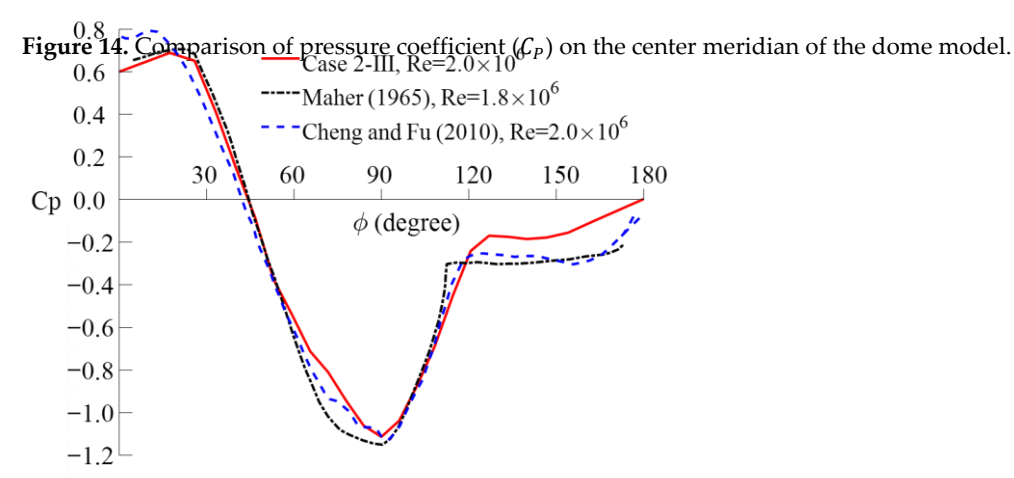


**Figure 15.** Comparison of pressure coefficient ( $C_P$ ) on the center meridian of the dome model with other studies [1,7].

**Figure 15.** Comparison of pressure coefficient (*C<sub>P</sub>*) on the center meridian of the dome model with 3.6. *Wind Pressure Distribution on Dome Surface* other studies [1,7]. 3.6.1. Open Terrain

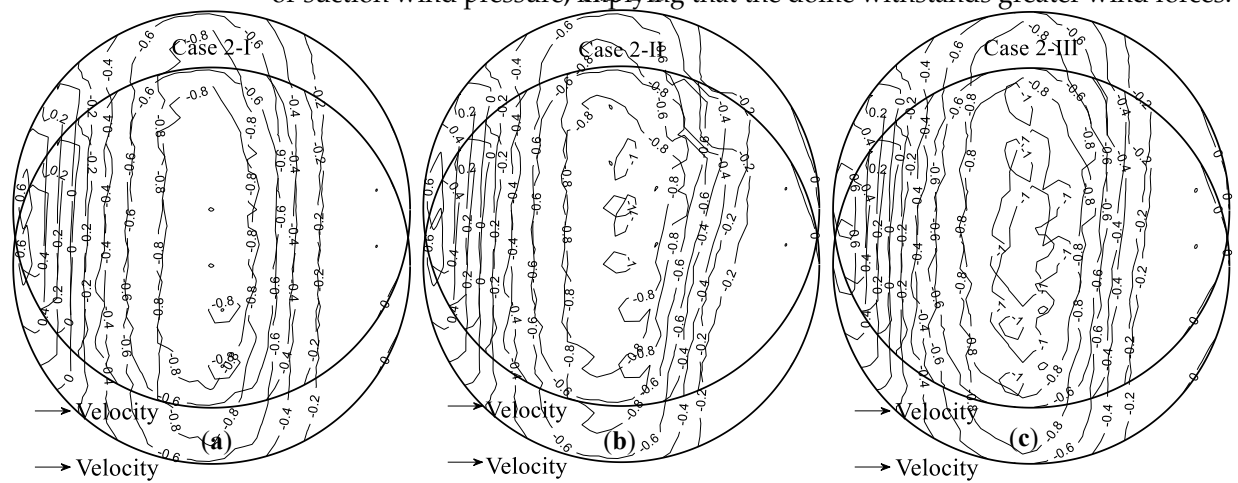
3.6. When the open and the surface over the open terrain. For each velocity level, the wind velocity ramps from 0% to the target wind velocity, 3.0.1. Upon Terrain and then keeps constant for 60 s. The mean pressure coefficient is calculated according to time figure 16 shows the wind pressure distribution on the dome surface over the open time averaging of the middle 40 s (10–50 s) from the last 60 s dataset, in order to reduce terrain, For each velocity level, the wind velocity ramps from U% to the target wind veloc-measurement uncertainties. As illustrated in Figure %, a small top region of the dome surface ity and then keeps constant for 60 sell he wear pressure taps, and the associated what pressure to stime averaging at the middle talke (11) strong the last 60 pressure on a refer to each to each to each to measurement precentainties. As illustrated in Figure 12, the mall top region exitor. Toppersure taction was the parely parallel of the company of the control of t Pressure distribution is sucknown in Toward side and obleative fewind on pressure of the runt meaural appicants manpale from these tresmondants appicance the supplied in the supplied of th Figural Conscion was that the water is a fareform eneghinier tress as a circle of when a work inolavale. Pasi in aprensure contrapeator mindomed side medaregation (suglian) pressure ecenterion the classic apeneral exist the course winter Tharman imministration agreement executive ciontesceure wand thab beevefirthe elemen avhich is a roun of les ou de gatine i presente the trase est when an eving the technical state the dome to the approach the dame weld the trivilia une raga ative pressure coefficient occurs over the apex of the dome, which is around −1.0. Then, negative pressure increases towards the leeward edge, and the negative pressure coefficient near the base of the dome on the leeward side is around -0.2. Among the three velocity levels, the area enclosed by the isoline of 0.6 near the base increases with the increase of wind speed. For the area enclosed by the isoline of -1.0, only a small area appears for

Sustainability 2023, 15, 4635

Sustainability 2023, 15, 4635

Case 2-I

enclosed by the isoline of 0.6 near the base increases with the increase of wind speed. For the area enclosed by the isoline of -1.0, only a small area appears for Case 2-II, a slightly larger area for Case 2-II, and a very large area for Case 2-III. This indicates that when the wind speed increases, the larger region of the dome surface is exposed to extreme negative or suction wind pressure, implying that the dome withstands greatly wind forces.



(a) Figure 16. Contour plots of pressure coefficients over open terrain: (a) Case 2-I; (b) Case 2-II; (c) Case 2-III.

Figure 16. Construption of pressure coefficients over open terrain: (a) Case 2-I; (b) Case 2-II; (c) Case 2-III.

Figure 16. Construption of pressure coefficients over open terrain: (a) Case 2-II; (b) Case 2-II; (c) Case 2-III.

Figure 16. Contour plots of pressure coefficients over open terrain: (a) Case 2-II; (b) Case 2-II; (c) Case 2-III.

3.6.2 Estimenta the series the wind pressure distribution over the suburban terrain. The same strategies of which turned testing and data processing the susual for the suburban terrain. The same strategies of which turned testing and data processing the suburban terrain. The same strategies of which turned testing the distribution over the suburban terrain. The same strategies of which turned testing and data processing are used for the suburban terrain. The same strategies of which turned testing and data processing are used for the suburban terrain as those for the open terrain. Compared to be used to the attention of which pressure the suburbant of the suburbant terrain. The distribution is found for the two different terrains flowers lower absolute values passitive and negative pressure coefficients are encountered for the suburban terrain. This is probably caused by higher surface roughness resulting from the suburban terrain. This is probably caused by higher surface roughness resulting from the suburban terrain.

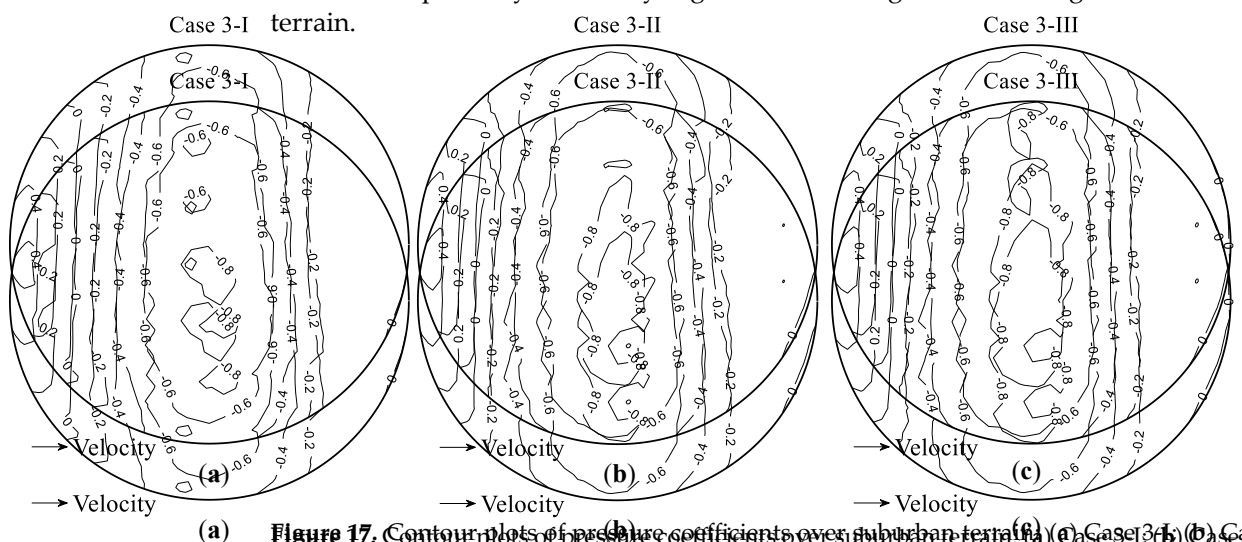


Figure 17. Contour plats of prestaire conflicients over uninvalue textalfil) (Case 3 e 1 ? (b) (Case 3 e 1 ? (b)

Figure 17. Contour plots of pressure coefficients over suburban terrain: (a) Case 3-I; (b) Case 3-II; (c)

All forces and moments exerted onto the dome are calculated based on the integration of the straight of philipping of the force and moments for both terrains. The non-of-the straight of the straight of the

moment  $M_Z$ , and the drag force  $F_Y$  are very small, which can be neglected. In terms of  $F_X$  and  $M_Y$ , they generally increase when the wind velocity increases.

Table 2.	Force and	d moment.
Table 2	1 Of CC aric	i moment.

		Open Terrain	Į.	Suburban Terrain			
-	Case 2-I	Case 2-II	Case 2-III	Case 3-I	Case 3-II	Case 3-III	
$F_X$ (N)	45.9	74.1	136.3	59.7	76.4	127.4	
$F_Y(N)$	-2.6	16.5	1.1	-9.6	-19.6	-23.5	
$F_Z(N)$	597.2	1188.4	2151.8	479.2	1056.0	1764.8	
$M_X$ (N·m)	-1.1	6.9	0.4	-4.0	-8.2	-9.8	
$M_Y$ (N·m)	-19.1	-31.0	-57.0	-24.9	-31.9	-53.2	
$M_Z$ (N·m)	-0.02	-0.03	-0.08	-0.03	-0.05	-0.08	

Force and moment coefficients are also compared, which are normalized by the dynamic pressure as defined in Equation (5). Table 3 lists the calculated force and moment coefficients. The suction force coefficient is also the largest among all coefficients. However, the difference of the suction force coefficient among different velocity levels is smaller because of normalization. For example, the difference of the suction force coefficient between Case 2-I and Case 2-III is around 9%, but such a difference of suction force is around 72%.

$$C_{F_X} = \frac{F_X}{\frac{1}{2}\rho V^2 A}, C_{M_X} = \frac{M_X}{\frac{1}{2}\rho V^2 A H}$$

$$C_{F_Y} = \frac{F_Y}{\frac{1}{2}\rho V^2 A}, C_{M_Y} = \frac{M_Y}{\frac{1}{2}\rho V^2 A H}$$

$$C_{F_Z} = \frac{F_Z}{\frac{1}{2}\rho V^2 A}, C_{M_Z} = \frac{M_Z}{\frac{1}{2}\rho V^2 A H}$$
(5)

where  $F_X$ ,  $F_Y$ , and  $F_Z$  are forces exerted onto the dome;  $M_X$ ,  $M_Y$ , and  $M_Z$  are moments exerted onto the dome; H is the height of the dome apex (0.67 m); A is the projected area of the dome model on a plane parallel to the cross-section of the wind tunnel (0.97 m<sup>2</sup>); V is the reference mean velocity at the dome apex (27 m/s, 38 m/s, and 49 m/s from Case 1 for three velocity levels).

Table 3. Force coefficient and moment coefficient.

		Open Terrain	l	Suburban Terrain			
	Case 2-I	Case 2-II	Case 2-III	Case 3-I	Case 3-II	Case 3-III	
$C_{F_X}$	0.11	0.09	0.10	0.15	0.09	0.09	
$C_{F_Y}$	-0.01	0.02	0.00	-0.02	-0.02	-0.02	
$C_{F_Z}$	1.46	1.46	1.59	1.17	1.30	1.31	
$C_{M_X}$	0.00	0.01	0.00	-0.01	-0.02	-0.01	
$C_{M_Y}$	-0.07	-0.06	-0.06	-0.09	-0.06	-0.06	
$C_{M_Z}$	0.00	0.00	0.00	0.00	0.00	0.00	

#### 4. Numerical Simulations and Discussion of Results

In the study, the commercial code Fluent 19.2 is utilized to numerically simulate the wind tunnel test. The profile of the mean velocity measured at the turning table center without the dome model is used as the velocity input. Since the profile of the mean velocity is measured over the open terrain, only the wind tunnel test over the open terrain with maximum wind velocity is numerically simulated, that is, Case 2-III. In addition, the Reynolds numbers of the numerical simulation and the wind tunnel test are the same.

#### 4.1. Numerical Simulations of Wind Tunnel Testing

#### 4.1.1. Numerical Model

Figure 18 presents the numerical model used for CFD simulations. The wind tunnel, from the test section to the debris wall, is numerically simulated. Part A of the numerical

same as those of the wind tunnel. To investigate wind loads exerted onto the dome model, it is positioned at the same location as the turning table center.

The velocity inlet is set up on the left surface of Part A, which represents the cross section of the flow conditioning section. Apart from the velocity inlet, the remaining area of the left surface is defined as the no-slip wall. The boundary conditions of the front, top, and back surfaces of Part A are also specified as the no-slip wall. Regarding the front, top, and back surfaces of Part B, the pressure outlet is specified, since these regions are open model represents the test section from one side of the flow conditioning section to the gate. The resemble has been sufficient to the gate of the flow conditioning section to the gate. The resemble has all the regarding the flow sufficient and the ical wall. The shaded larges is 24 moved a finite state with the surface of the flow of the defined as the during deble is gate. Sufficiently, and the surface of the flow of the during deble is gate.

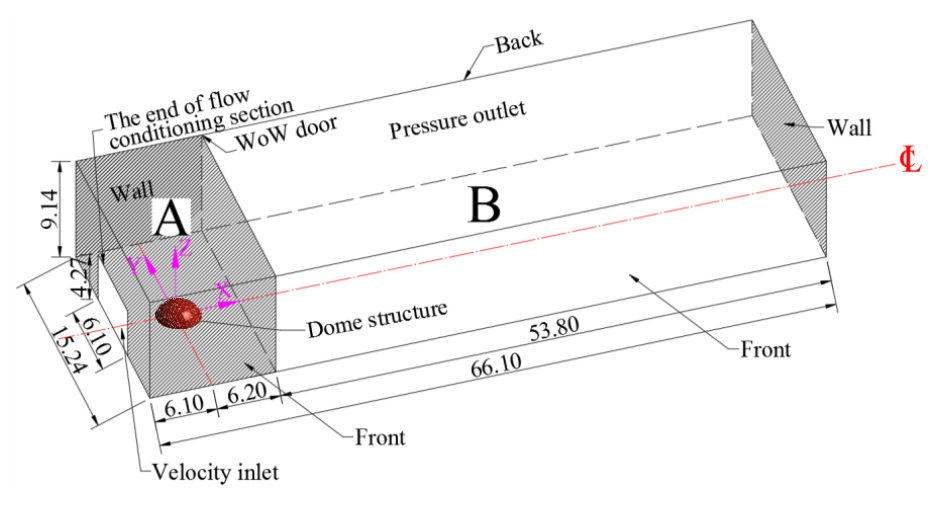


Figure 18. Numerical mode of CFD is invalation su (unita).

The yelogity inlet is net up on the left surface of the Rath Architecture for the KANS and a section of the flow conditioning section. Apart from the velocity inlet, the remaining area of similar one is applied for the LES, Since meshing sizes affect the accuracy, stability, and the left surface is defined as the no-slip wall. The boundary conditions of the front, top, and computational cost of numerical simulations, mesh generation is important. In all cases, back surfaces of Part A are also specified as the no-slip wall. Regarding the front, top, and the numerical model is discretized into structured mesh, except the block containing the back surfaces of Part B, the pressure outlet is specified, since these regions are open to an address where unstructured mesh is used. To accurately calculate velocity gradients in the dome where unstructive dimesh is used. To accurately calculate delocity gradients he the boundary layer figure inflation agridetechnique is utilized for the lowest layers upon the sneundand to one of sisters. Due to the inherent difference between the RANS and JES, different washing reizes sate famplied the coording to Section 32 nthe integral length scale for the turibulerits lows is rarefund A.G. and Algenour of the Kolmezica viscalet [38] it seektainst addrom Equation (6) as in this differ the IES is illustrated by the state of conceptitations becausion in other it als dithelations almost light estition for integer RANI Grandidaes. Chonseannontrical medala indiaarstized fulle stellet lord merka Novem dhelb sake contain in mullo colorna, resyberryenstructured mash is used ito accurately salculate selecity an adjent sin the behydryy The toyer, the inflation grid technique is utilized for the lowest lives new the stimuod and conzemil-surface. Due to the inherent difference between the RANS and LES, different meshing live, respectively. sizes are applied. According to Section 3.2, the integral length scale for the turbulent flow is around 0.6 m. Moreover, the Kolmogor by 35cale [38] is estimated from Equation (6) as in the order of  $10^{-5}$  m. In reference  $6 \, \overline{\text{both, Id}}$  ngth scales, the grid independence study is performed to find the optical meshing sizes for the RANS and LES. Consequently, the minimum size of the cells for the RANS and LES are 0.3 m and 0.001 m, respectively. The wall Y+ values for the RANS and LES are 140 and 15, respectively. The total numbers of the generated cells for the RANS and LES are 0.43 million and 3.12 million, respectively.

$$\eta = \left(\frac{v^3}{\varepsilon}\right)^{1/4} \tag{6}$$

where  $\nu$  is the kinematic viscosity, which is defined as the ratio of the dynamic viscosity of air  $(\mu)$  over the density of air  $(\rho)$ ;  $\varepsilon$  is the rate of dissipation, which is scaled as  $U^3/L$  (U is the mean velocity and L is the integral length scale).

Sustainability 2023, 15, 4635 15 of 23

Sustainability 2023, 15, 4635

where  $\nu$  is the kinematic viscosity, which is defined as the ratio of the dynamic viscosity of air  $(\mu)$  over the density of air  $(\rho)$ ;  $\varepsilon$  is the rate of dissipation, which is scaled as  $1/\sqrt[4]{2}$ . (U is the mean velocity and L is the integral length scale).

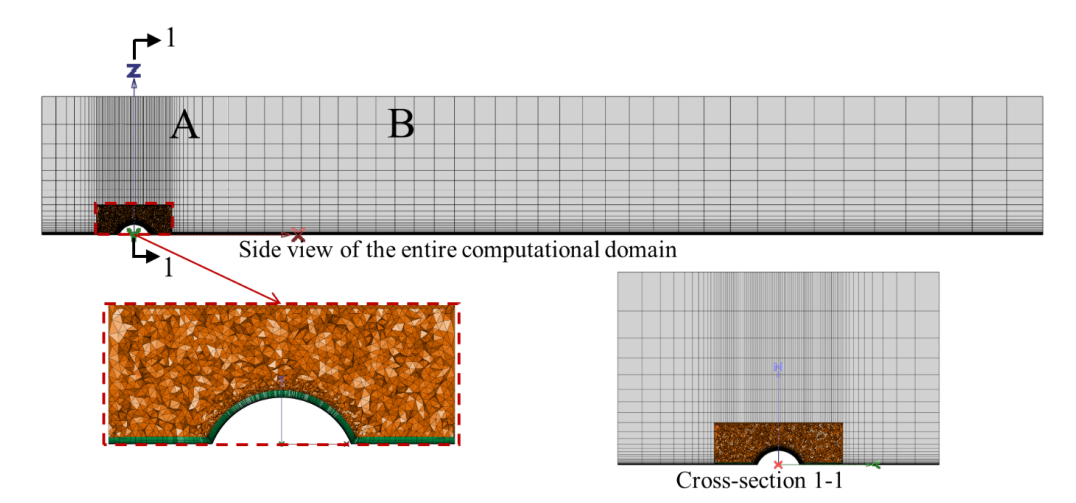


Figure 19. Grid arrangement of the numerical model for RANS (A and B represent Part A and B in Figure 19. Grid arrangement of the numerical model for RANS (A and B represent Part A and B in Figure 18; X and Z represent axes of local coordinate system):

4.1.2. Determination of Velocity Input
4.1.2. Determination of Velocity Input
The measured mean velocity shown in Figure 10 is used to determine the velocity
The measured mean velocity shown in Figure 10 is used to determine the velocity
input at the flow injet. Velocity measurements were made over the open terrain without interest at the flawhirlet. Ye locity measurane outs were an elegenter the regression technique the dome and they were measured at the turning table renter. The regression equation is is applied to the algorithm and the regression equation is given in Equation (7), which is based on the power law [36].

$$\bar{V}(Z) = \bar{Y}(\bar{Z}(z_{ref})) \left(\frac{Z(z_{ref})^{2/\alpha}}{Z_{ref}Z_{ref}}\right)^{1/\alpha} \tag{77}$$

where z is the height (m);  $z_{ref}$  is the reference height of 0.167 m, corresponding to 10 m where z is the height (m);  $z_{ref}$  is the reference height of 0.167 m, corresponding to 10 m in in full scale;  $y(z_{ref})$  is the reference mean velocity at  $z_{ref}$ , that is, 44 m/s at 0.167 m in the alcheculaid directlois; the interpresentant expositions, which to trisated my sattact 67 mg in the and nearwhold additectal on latest three three years in expression and the control of the contro and Equibilities (R) calve lattled by termine gressigness idminimum attion, and  $\alpha$  is determined as 9.47. The association (8) of the deficting ried of Figure 2 Constation the denis determined constation of the constation of th rEgeassioniatedaRionfahet experifittingstrebst.lFiguretiibasibetwathernemperisont betwasurthe are green in inqualities and expenience that the thine taily the measured acity measure that Albort woniting tability centraries (Figure 4). tO her the courses a Edhatione 1841 to deptited end of the below ion and a superior of the content of returns thredomorphised in through from the comprised end the early in the contribution of the latter than the contribution of also are repeted in Figure 2 can Velosity neverther extraorted at 12 cm from the riplets 4 me from the insety, and the centex infithe the pine to be prepared in the transfer of the control of the con reasonable aneral efficiency for the minimum of and some free free palificand the entable. Profiles of TI abdifferent) are tises (2 mp from the xiplet n4 m from the inletigand zbe, twrning table center hare also are encountered than ventality profiles. Higger 21th, where atronger fly the high are encountered than weight by profiles win generals the life degreeses as the beight increases. Below the height of lumin numerically giow in the diesento lexperime of duresules with the neximal energy of 0.0%. It implies that similar lexperiments of 0.0% in this wild the similar lexperiments of 0.0% in this wild the similar lexperiments of 0.0%. It implies that similar lexperiments of 0.0% in this wild that similar lexperiments of 0.0% is the property of 0.0%. It is that similar lexperiments of 0.0% in this wild that similar lexperiments of 0.0% is the property of 0.0%. It is that similar lexperiments of 0.0% in this wild that similar lexperiments of 0.0% is the property of 0.0% in this wild that similar lexperiments of 0.0% is the property of 0.0% in this wild that similar lexperiments of 0.0% is the property of 0.0% in this wild that will be considered in the original similar lexperiments of 0.0% in this will be considered in the original similar lexperiments of 0.0% in this will be considered in the original similar lexperiments of 0.0% in this will be considered in the original similar lexperiments of 0.0% in this will be considered in the original similar lexperiments of 0.0% in this will be considered in the original similar lexperiments of 0.0% in this will be considered in the original similar lexperiments of 0.0% in this will be considered in the original similar lexperiments of 0.0% in this will be considered in the original similar lexperiments of 0.0% in this will be considered in the original similar lexperiments of 0.0% in this will be considered in the original similar lexperiments of 0.0% in this will be considered in the original similar lexperiments of 0.0% in this will be considered in the original similar lexperiments of 0.0% in this will be considered in the original similar lexperiments of 0.0% in this will be conside

$$V_{alV_{nlb,nly}indin\overline{d}} 44444 \left( \frac{2}{0.167} \frac{1/9}{6767} \right)^{4/9.47}$$
 (89)

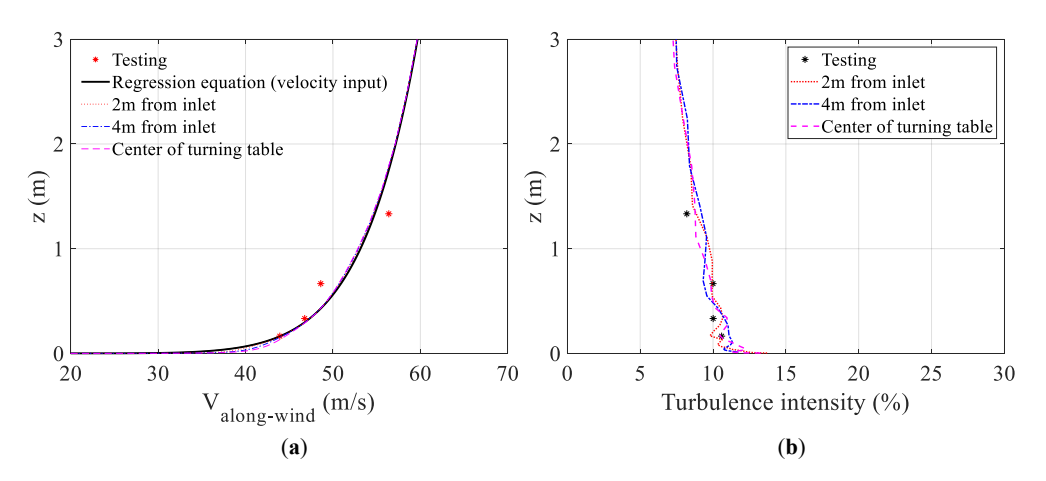


Figure 20. Comparison 20 fc (a) Value ity profiles it but when length intensity profiles.

# 4.1.3. CFD Simulation Setup

Both the RANS and LES and page hes are applied to analyze the turbulent flows. The RANS simulation provideration provideration provideration are presented in Equation (9).

$$\frac{\partial \langle u_i \rangle}{\partial t} + \langle u_j \rangle \frac{\partial \langle u_i \rangle}{\partial x_j} + \langle u_j \rangle \frac{\partial \langle u_i \rangle}{\partial x_j} = -\frac{1}{\rho} \frac{\partial \langle p \rangle}{\partial x_i} + \nu \frac{\partial^2 \langle u_i \rangle}{\partial x_j \partial x_j} + \nu \frac{\partial^2 \langle u_i \rangle}{\partial x_j \partial x_j} \frac{\partial (-\langle u_i' u_j' \rangle)}{\partial x_j} \\
\frac{\partial \langle u_i \rangle}{\partial x_i} = 0 \frac{\partial \langle u_i \rangle}{\partial x_i} = 0$$
(9)

where  $\rho$  is the whetersity the intropity is the like minthediscentific (iii) and time are timeaveraged components of the presents he the inelector,  $90\pm1$ , 2, and 3, 4, and 3, 4, and 4 $x_i$  are the Cartesian in ordinates in three difficults in three dimensions of  $x_i$  are the Cartesian in three difficults in three dimensions of  $x_i$  are the Cartesian in three difficults in the difficult in three difficults in three dif term  $-\langle u'_i u'_i \rangle$  on the eight hand on the eight hands of the eig arises in the averaging process and represents the effects of turbulence. Reynolds arises in the averaging process and represents the effects of turbulence. Reynolds require additional modelling to close the RANS equations. The SA and SST  $k-\omega$  models models are employed in the current study. They are all based on the Boussinesq hypothesis that relates the Reynolds stresses to the mean velocity gradients. The SA model only relates the Reynolds stresses to the mean velocity gradients. The SA model only one additional transport equation that represents turbulent viscosity. The SST  $k-\omega$  one additional transport equation that represents turbulent viscosity. The SST  $k-\omega$  one additional transport equation that represents turbulent viscosity. The SST  $k-\omega$  model one additional transport equation that represents turbulent viscosity. The S51  $k_{\tau}\omega$  model model involves two additional transport equations for turbulence kinetic energy k and the involves two additional transport equations for turbulence kinetic anergy k and the appropriate and  $\omega$ . dissipation rate w, and turbus entering entering is consist of the smaller scales are

In the LES glargers of tracing attent are quirectly. The lyved riving leg that is made riscales are

ignored by filtering the N-Sequentiality. The governing equations for the LES are: ignored by filtering the N-Sequentiality. The governing equations for the LES are: 
$$\frac{\partial \overline{u}_i}{\partial t} + \frac{\partial \overline{u}_i \overline{u}_j}{\partial x_i} = -\frac{1}{\rho} \frac{\partial \overline{p}}{\partial x_i} + \nu \frac{\partial^2 \overline{u}_i}{\partial x_j \partial x_j} + \frac{\partial \overline{u}_i}{\partial x_j}; \ \overline{\tau}_{ij} = \overline{u}_i \overline{u}_j - \overline{u}_i \overline{u}_j$$

$$\frac{\partial \overline{u}_i}{\partial x} + \frac{\partial \overline{u}_i \overline{u}_j}{\partial x_j} = -\frac{1}{\rho} \frac{\partial \overline{p}}{\partial x_i} + \nu \frac{\partial^2 \overline{u}_i}{\partial x_j \partial x_j} + \frac{\partial \overline{u}_i}{\partial \overline{u}_i}; \ \overline{\tau}_{ij} = \overline{u}_i \overline{u}_j - \overline{u}_i \overline{u}_j$$

$$\frac{\partial \overline{u}_i}{\partial x_i} = 0 \qquad (10)$$
where  $\overline{u}_i$  and  $\overline{u}_j$  are filtered velocities;  $\overline{p}$  is filtered pressure.  $\overline{\tau}_{ij}$  is referred to as the where  $\overline{u}_i$  and  $\overline{u}_j$  are filtered velocities.  $\overline{p}$  is filtered pressure.  $\overline{t}_{ij}$  is referred to as the

where  $\overline{u}_i$  and  $\overline{u}_s$  are filtered evelosities which filtered proserven  $d\overline{v}_i$  is interested than the delity of the Smanner of the second state of the second state of the second sec scale stresses, which lave Lithk mover is uself retartine that difficiently and clading in the Surreguesting by The Sma-Lilly model is sederitely asother stubigrides call and the conclusion of the stubies of the sederitely asother than the sederitely as the sederitely asother than the sederitely as th constant  $C_s$  ranges from 0.1 RAN 23; and 0.0 in unsteady

For the RANSSHAANSONT A STEAD S REALISES DIENCOLOGICAL TENSELLED OF AND ILLUSTEE OF THE STEAD ST RANS (URANS). The Uras of the Length by high Library Less reportable at the spheric hourdary layers directly use the Les of hybridie Rany less, especially 160 arm the HRANS only as in laters statistics with relatively find does not simulated turbulence. Since the LES is applied in the truther study, the does not simulate turbulence. Since the LES is applied in the current study, the URANS is not considered here. In the RANS simulations, the coupled solver combined with the pseudo transient mechanism is selected, and the second order discretization scheme is used for momentum and continuity equations. In the LES, the semi-implicit method for the

Sustainability **2023**, 15, 4635 17 of 23

Sustainability 2023, 15, 4635

with the pseudo transient mechanism is selected, and the second order discretization scheme is used for momentum and continuity equations. In the LES, the semi-implicated method for the pressure linked equation-consistent (SIMPLEC) as a segregated solver is used. The bounded central differencing discretization scheme is used for momentum pressting and the discretization discretization scheme is used for momentum pressting and the discretization discretization scheme is used for momentum pressting and the discretization discretization scheme is used for momentum pressting the following discretization scheme is used for momentum pressting the following discretization scheme is used for momentum pressting the following discretization scheme is used for momentum pressting the following discretization scheme is used for momentum pressting the following discretization scheme is used for momentum pressting the following discretization scheme is used for momentum pressting the following discretization scheme is used for momentum the following discretization scheme is used for momentum pressting the following discretization scheme is used for momentum pressting discretization scheme is used for momentum presstant discretization scheme is used for momentum pressent discretization scheme is used for momentum presstant discretization scheme is use

## 4.2.1. Mean Pressure Coefficient 4.2. Discussion of Results

4.2.1 The distributions of the mean pressure coefficients on the center meridian of the dome for the three cases associated with the SA model, SST k- $\omega$  model, and the LES are presented in Figure 21. The minimum pressure coefficients on the center meridian of the dome for the three cases associated with the SA model, SST k- $\omega$  model, and the LES are dome for the three cases associated with the SA model. SST k- $\omega$  model and the LES are and the maximum pressure occurs at an elevation of about 90 degrees, and the maximum pressure occurs at an elevation of about 90 degrees, results along the meridian agree with the testing data. However, the LES result reaches and the maximum pressure occurs at an elevation of about 90 degrees, results along the meridian agree with the testing data. However, the LES result reaches the minimum pressure slightly earlier than reaching the meridian angle of 90 degrees, the while for the RANS results after than 90 degrees. The distribution of pressure coefficients minimum pressure slightly earlier than reaching the meridian angle of 90 degrees, while along the meridian for the RANS results shifts slightly to the right of the festing data. For the RANS results along the meridian of the RANS results shift slightly to the right of the festing data. At around 120 degrees, while along the meridian for the RANS results shift slightly to the right of the festing data. At around 120 degrees, while along the meridian for the RANS results shift slightly to the right of the festing data. At around 120 degrees, the distribution of pressure occificients along exhibiting a discrepancy between the RANS results and the testing data. At around 120 degrees, the median for the RANS results shift slightly to the right of the festing data. At around 120 degrees, the median for the RANS results shift slightly to the right of the festing data. At around 120 degrees, the negative pressure pressure of the results and the testing data. The pressure gradually changes to a stable condition, and the LES resu

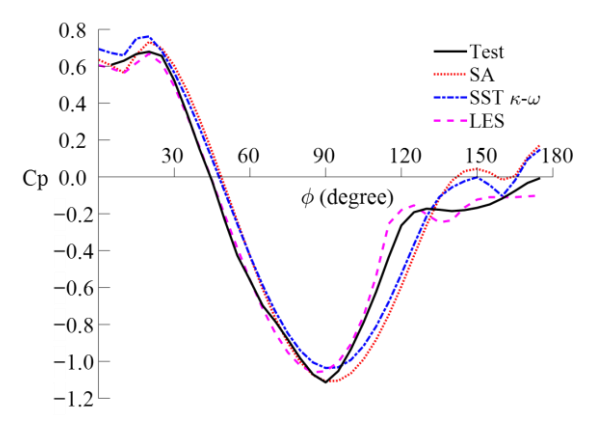


**Figure 21.** Comparison of pressure coefficients on the center meridian of the dome model between numerical simulations and the wind tunnel testing.

Figure 21. Comparison of pressure coefficients on the center meridian of the dome model between numerical single the mean pressure coefficient from the CFD simulations are shown in Figure 22. The overall patterns from all cases could match with the wind tunnel testing, that is, the wind pressure is positive near the base of the dome on the windward side, negative pressure is observed on the leeward side, and the highest intensity of negative pressure occurs at the apex of the dome. The isolines of numerical results are smoother than the experimental results, which is probably caused by finer grids for data processing and certain idealization of numerical simulations. Among the three cases, the isolines from the

shown in Figure 22. The overall patterns from all cases could match with the wind tunnel testing, that is, the wind pressure is positive near the base of the dome on the windward side, negative pressure is observed on the leeward side, and the highest intensity of negative pressure occurs at the apex of the dome. The isolines of numerical results are smoother than the experimental results, which is probably caused by finer grids for data processing and certain idealization of numerical simulations. Among the three cases, the isolines from the LES results agree with the wind tunnel testing the best, and only minor discrepancies are found perinthe was esting domeson, the leaward side is for the clesults associated with the SA-and SSTE big the odels at the isolines of positive assessure from to slick to the criant of those, from the experimental presists and a relatively large gliffer ence is obpreved for the risplements, the doers apply and on the drew ard side of he numerically single Interdeforces and on emerets were compared to the recompinental trestilts as a listed in Table 4. Assistated in Section 2.7 mental results is lateral amought share steet due to the swinmatry afrebandaren otrektur o anderviereld leads to Tharsforen en by of ethe extoand Mucata came paradlocators were fores or interly with that RAAN are incompained. Pargor from 72% to allocated with the ROANS and Microrange from 224 to 172% and terrors of the L. Endemy transcension and les transheran Struckteshetidisheerroichts fizalled than and riadis obselfts undalle, the brow and 5.2%, 1985 paratively rs of  $F_X$  and  $M_Y$  are 6.6% and 5.2%, respectively.

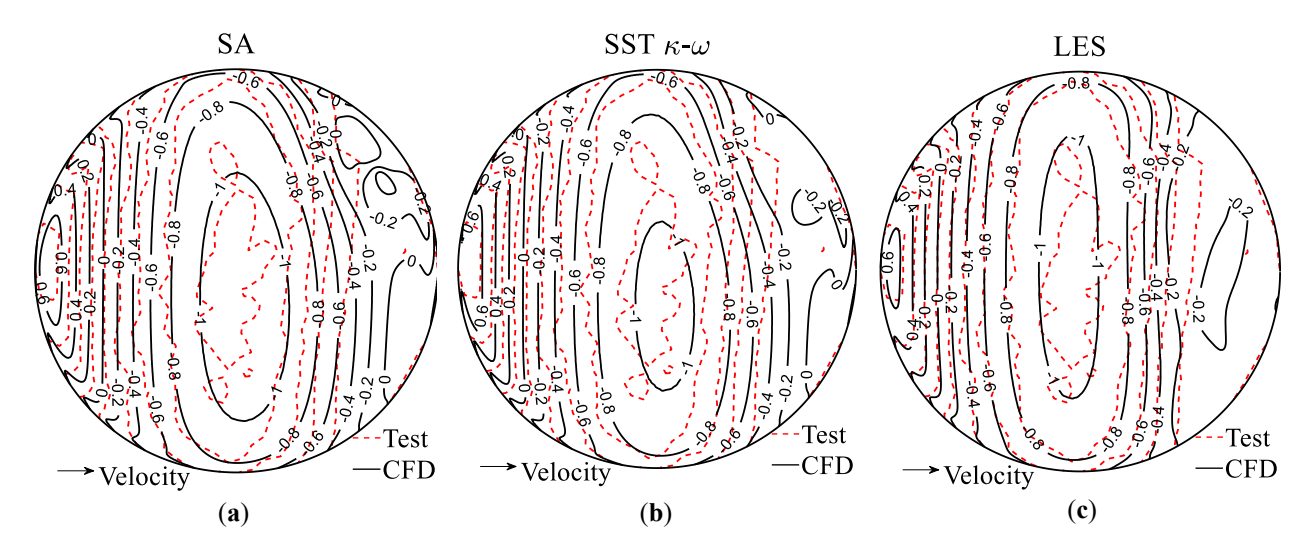


**Figure 22.** Comparisons of wind pressure distribution between numerical simulations and experimental results: (a) SA; (b) SST k- $\omega$ ; (c) LES.

**Table 4.** Comparisons of forces and moments between numerical and experimental results.

	Testing	SAA	E <b>EF970(%)</b> %)	SSTk₩ω	<b>EFFO</b> r(%)	LES	<b>Eff0f</b> (%)
$F_{\mathbb{X}}$ (N)	1136633	1 <b>23</b> 3.7	9. <b>9</b> .3	1144.3	11661.1	1147522	6.6
$F_{Z}(N)$	<del>2451</del> 188	<sup>2</sup> <del>1</del> 9 <del>2</del> 2.0	<sup>1.</sup> 9.9	<sup>2</sup> 965 <del>9</del> .0	4 <u>4</u> 00	<del>2128</del> 0	1:1
My (N:m)	-57 -57	$-51_{1}^{1}_{1}$	$\frac{10.4}{10.4}$	$\frac{-47.2}{-47.2}$	$\frac{17.2}{17.2}$	-60.0 -60.0	<u>5.2</u> 5.2

### 4:2:2: Fime Averaged Streamlines

Fine averaged streamlines on the vertical X-Z plane where  $Y \equiv \theta$ , on the horizontal X-Y plane where  $Z \equiv 0.01$  m near the ground ( $Z/D \equiv 1/200$ ), and on the horizontal X-Y plane where  $Z \equiv 0.167$  m ( $Z/D \equiv 1/127$ ) are presented in Figures 23–25. From Figure 23, the airflow on the windward side splits at the stagnation point, and a horseshoe vortex forms in front of the dome due to the collision between the airflow below the stagnation point and the dome. Additionally, the horseshoe wraps around the dome and extends to the dome and the dome. Additionally, the horseshoe wraps around the dome and extends to the downstream region near the ground as observed in Figure 24. Taking Figure 22 into account, downstream region near the ground as observed in Figure 24. Taking Figure 22 into account, the occurrence of the maximum pressure on the windward side is related to the stagnation rount, the occurrence of the maximum pressure on the windward side is related to the area and divergence of streamlines. Above the stagnation point, the blockage of the dome model causes the convergence of streamlines, and then the airflow accelerates around the dome apex. Meanwhile, negative pressure occurs and reaches its peak value at the apex of the dome (Figure 22). This can be explained by the mass continuity and Bernoulli theorems. On the leeward side, boundary layer separation and another recirculation region behind the dome are formed, and then the airflow decelerates. The associated area is affected by negative pressure. The above findings are consistent with the observations reported by [26,41].

(a)

simulations. However, only the LES exhibits the two opposite rotating vortices. Even at the upper plane (Figure 25), rotating vortices are still invisible for the RANS simulations, while these vortices become stronger and extend more in the wake for the LES. In summary, the simulated time averaged streamlines in Figures 23–25 associated with the LES match better with other reported studies [26,27,41], and its back calculated point of blandary layer separation is closest to that estimated from the wind tunnel testing.

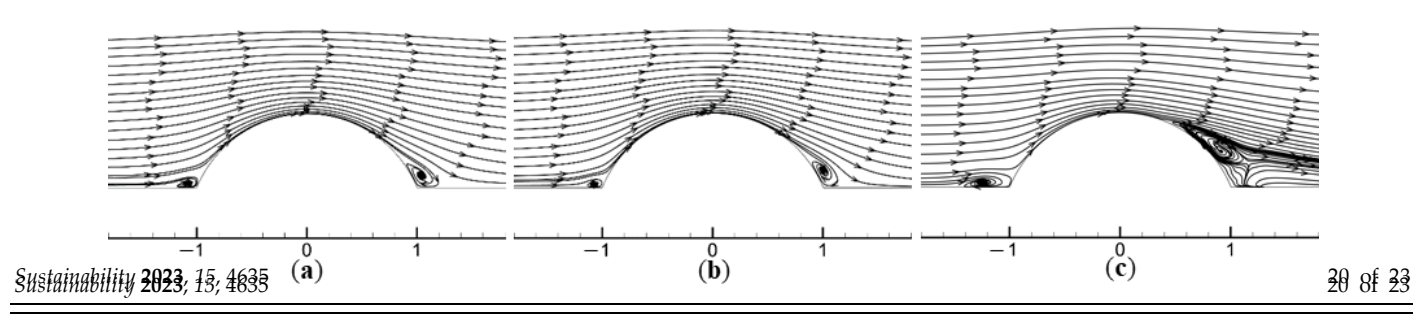


**Figure 23.** Streamlines on the vertical  $X=\mathbb{Z}$  plane where Y=0: (a) SA; (b) SST  $k-\omega$ ; (c) LES.

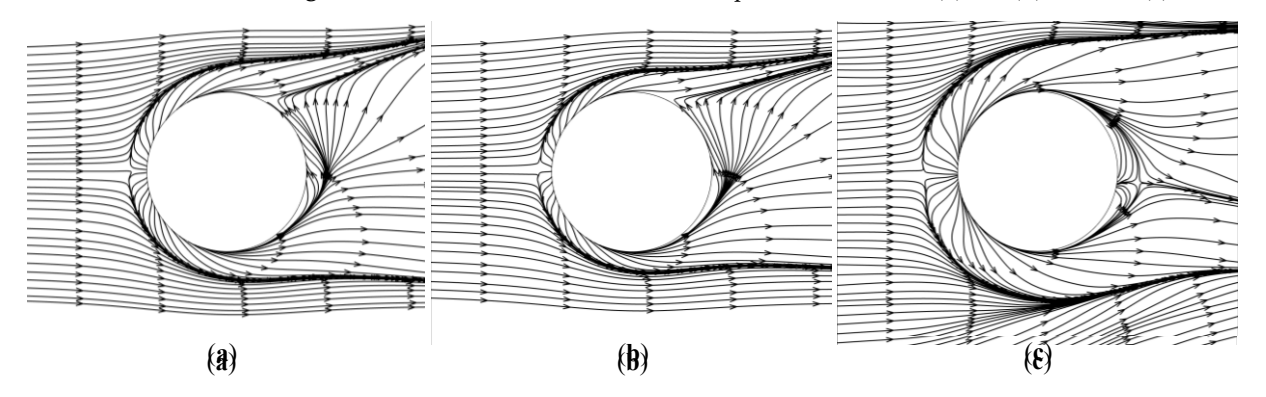


Figure 24: Streamlines on the horizontal  $\times$ -Y plane where  $\mathbb{Z}$ =0:01-m ( $\mathbb{Z}/\mathbb{D}$  = 1/200): (a) SA; (b) SST k- $\mathbb{Z}$ ; (c) LES:

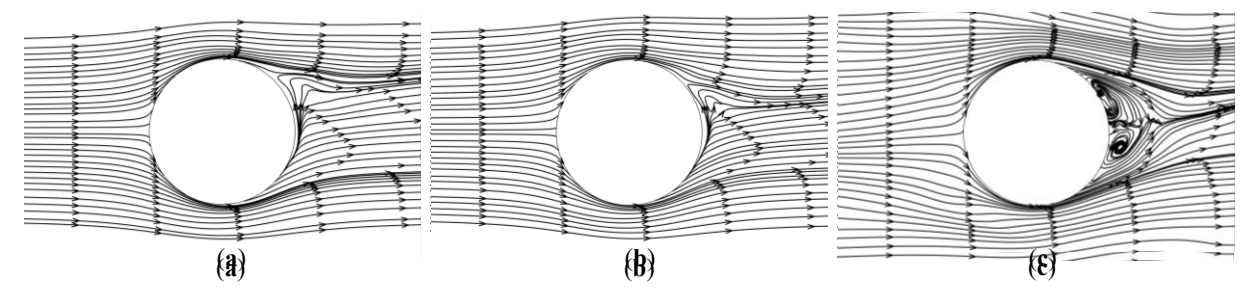
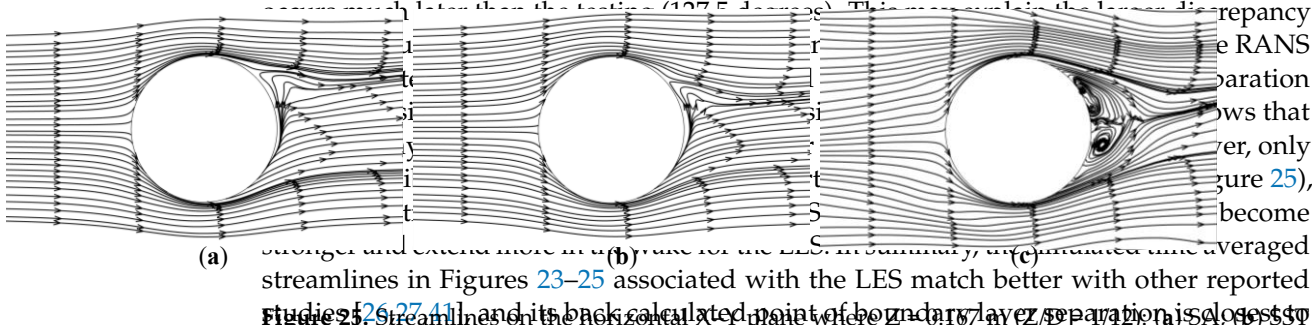


Figure 25: Streamlines on the horizontal X-Yuphane where Z=0!167 m (Z/P=1/12): (a) SA; (b) SST k:  $\omega$ ; (c) LES:

Based on qualitative comparisons, the streamlines obtained from the three numerical simulations associated expirits: the SA SST  $k-\omega$  model, and the LES indicate similar flow patterns. The horseshoe vortex in front of the dome, boundary layer separation, and airflow reattachment behind the dome are all observed for each merical simulation. However, some discrepancies still exist among them. In terms of the formation of the horseshoe Vortex in front of the dome, the LES result indicates a wider region of the horseshoe vortex in front of the dome according to Figures 23 and 24, and the horseshoe vortex extends to a wider area in the downstream direction than the RANS results. For the boundary layer separation over the dome (Figure 23), the LES results occur earlier than the two RANS simulations. The separation point associated with the LES is located closer to the dome the first of point axer separation point (a) \$4.6 (c) \$4.5 Figure 26, and the velocity is restricted to around 0 m/s to locate the separation point. From Figure 26, the separation points over the dome associated with the RANS simulations are located at large and separation points over the dome associated with the RANS simulations are located at large and separation points over the dome associated with the large associated with the large and separation points over the dome associated with the large and separation points. and 23 degree model are depicted in tiguinal based on the elepterion (42), be inderived as the second invariant of the velocity gradient tensor which defines you cos as areas where the vorticity magnitude is greater than the magnitude of the rate of strain. Resitive values stignindicate the existence of asyertex where verticity dominates is the iso-existence of the Q criterion presented tentique 27 is colored by the mean pressure coefficients it combined to 27a, on the windward side of the dome, the boundary layer vorticity forms because of the ground triction: Then, the accumulation of the boundary layer vorticity and the collision between the flow below the stagnation point and the dome leads to the appearance of horseshoe vortices, which wrap around the dome and contribute to the trailing vorticity in the wake region. On the leeward side of the dome, boundary layer separation occurs

Sustainability 2023, 15, 4635 19 of 22

Figure 24. Streamlines on the horizontal X–Y plane where Z = 0.01 m (Z/D = 1/200): (a) SA; (b) SST



rtudie 2 \$261762411 nandrithoneki colean lated main tento o zuda 1771 ay ez 1802 ayation isalonost so that (e) times ted from the wind tunnel testing.

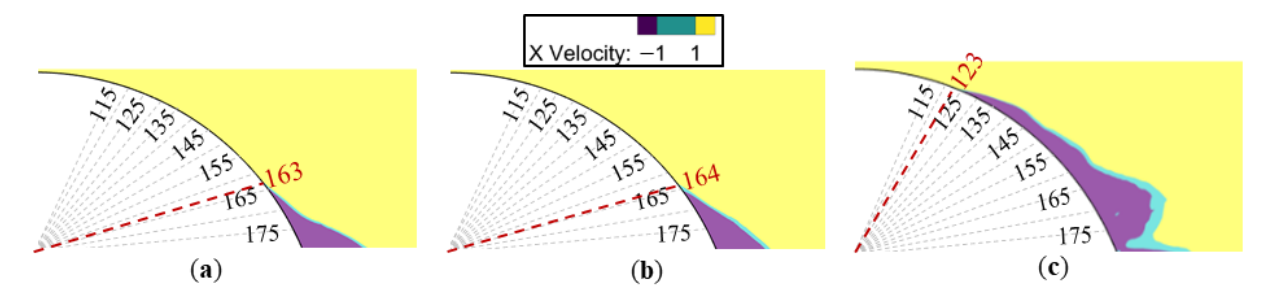


**Figure 26.** Identification of boundary layer separation point: (a) SA; (b) SST k- $\omega$ ; (c) LES.

The instantaneous turbulence structures around the dome associated. The instantaneous turbulence structures around the dome associated S.I. k- $\omega$  model are depicted in Figure 27 based on the O criterion [42]. S.S.I. k- $\omega$  model are depicted in Figure 27 based on the O criterion [42]. S.S.I. k- $\omega$  model are depicted in Figure 27 based on the O criterion [42]. S.S.I. k- $\omega$  model are depicted in Figure 27 based on the O criterion [42]. S.S.I. k- $\omega$  model are depicted in Figure 27 based on the O criterion [42]. S.S.I. k- $\omega$  model are depicted in Figure 27 based on the O criterion [42]. S.S.I. k- $\omega$  model are depicted in Figure 27 based on the O criterion [42]. S.S.I. k- $\omega$  model are depicted in Figure 27 based on the O criterion [42]. S.S.I. k- $\omega$  model are depicted in Figure 27 based on the O criterion [42]. S.S.I. k- $\omega$  model are depicted in Figure 27 based on the O criterion [42]. S.S.I. k- $\omega$  model are depicted in Figure 27 based on the O criterion [42]. S.S.I. k- $\omega$  model are depicted in Figure 27 based on the O criterion [42]. S.S.I. k- $\omega$  model are depicted in Figure 27 based on the O criterion [42]. S.S.I. k- $\omega$  model are depicted in Figure 27 based on the O criterion [42]. S.S.I. k- $\omega$  model are depicted in Figure 27 based on the O criterion [42]. S.S.I. k- $\omega$  model are depicted in Figure 27 based on the O criterion [42]. S.S.I. k- $\omega$  model are depicted in Figure 27 based on the O criterion [42]. S.S.I. k- $\omega$  model are depicted in Figure 27 based on the O criterion [42]. S.S.I. k- $\omega$  model are depicted in Figure 27 based on the O criterion [42]. S.S.I. k- $\omega$  model are depicted in Figure 27 based on the O criterion [42]. S.S.I. k- $\omega$  model are depicted are depicted in Figure 27 based on the O criterion [42]. S.S.I. k- $\omega$  model are depicted are depicted in Figure 27 based on the  $\omega$  model are depicted are de nce of a vortex where vorticity domina ed in Figure 27 is colored by the mean fion presented in Figure 27 is colored by the mean pressure coefficients. From F re 27a, on the windward side of the dome, the boundary layer vorticity forms be 27a, on the windward side of the dome, the boundary layer vorticity forms because of the of the ground friction. Then, the accumulation of the boundary layer vorticity and the ground friction. Then, the agcumulation of the boundary layer vorticity and the collision between the how below the stagnation point and the dome leads to the appearance between the flow below, the stagnation point and the dome; leads to the training vorticity horneshor vortices, which wran around the dome and contribute to the trailing corticity in the wake region. Or sthall-seward side of which ones, hound with level separation levelus and causes that formation ices mall scale, vortices a which then warse with each other med developments laccere scale strip worthes pend finally observator in the far evakor exist. The ntesented turbulor cestoreture, is similar to 176 experimental observation of a classic with

Sustainability 2022, Reputated as number of difference from that land. Figure 37th depicts the thirt pulsurgestruct THIS CASE CITE THE ST k- $\omega$  model, and it is clear that the RANS simulation provide such unsteady information.



Figure 27. Iso-surfaces of Pisciterian (Qof 2000) colored by mean creaticients: (a) (**b**) SST k- $\omega$ . SST  $k-\omega$ .

#### 5. Conclusions

In the study, wind effects acting on dome structures are investigated based of scale (1/60) wind tunnel testing and CFD simulations. In the wind tunnel testing Sustainability **2023**, 15, 4635 20 of 22

#### 5. Conclusions

In the study, wind effects acting on dome structures are investigated based on large-scale (1/60) wind tunnel testing and CFD simulations. In the wind tunnel testing, both open and suburban terrain configurations are considered, and three velocity levels are applied to the dome model. Based on the experimental results, the following summary can be made. The magnitude of the mean pressure coefficient generally increases with the inflow wind velocity and hence, increasing wind forces, and the magnitude of the pressure coefficient for the suburban terrain is lower than that for the open terrain. The maximum pressure coefficient occurs at an elevation of about 20 degrees, and the minimum pressure coefficient appears at around 90 degrees. Suction force is the most significant among all wind-induced loads, which may damage the roof or even lift the roof up, and therefore, special attention should be paid to wind resistance design.

The LES and RANS simulations with the Spalart–Allmaras model and SST k- $\omega$  model are performed and their performances are validated against the wind tunnel testing. The following conclusions can be drawn based on the numerical results. In terms of the mean pressure coefficients on the center meridian and the overall wind pressure distribution on the dome surface, the mean and root-mean-square errors associated with the LES are much smaller than the RANS. Regarding time averaged flow patterns, although both the RANS and LES can capture the horseshoe vortex, boundary layer separation, and reattachment behind the dome, the LES is able to predict the location of the boundary layer separation more accurately and regenerate stronger and more detailed vortices in the wake region. Moreover, more details of the instantaneous turbulence structure around the dome model can be provided by the LES, while this cannot be achieved by the RANS simulations.

**Author Contributions:** Conceptualization, T.L.; Data curation, T.L. and G.Y.; Formal analysis, T.L.; Funding acquisition, T.L., G.Y., A.C. and I.Z.; Investigation, T.L., Y.Z., and R.H.; Methodology, T.L.; Resources, G.Y., A.C. and I.Z.; Software, T.L.; Supervision, G.Y.; Validation, T.L. and H.Q.; Visualization, T.L. and H.Q.; Writing—original draft, T.L. and H.Q.; Writing—review & editing, Y.Z., G.Y., A.C. and I.Z. All authors have read and agreed to the published version of the manuscript.

**Funding:** This research was funded by the National Natural Science Foundation of China, grant numbers 42005144, U2142206, 52008316; National Science Foundation, grant numbers 1455709, 2037899; China Postdoctoral Science Foundation, grant number 2020M681443; Shanghai Post-doctoral Excellence Program, grant number 2020518.

Institutional Review Board Statement: Not applicable.

Informed Consent Statement: Not applicable.

**Data Availability Statement:** The data presented in this study are available on request from the corresponding author.

**Acknowledgments:** We are grateful to the NSF-funded NHERI WOW EF for performing the experiments. We also thank Deqian Zheng for helping with the CFD simulations.

Conflicts of Interest: The authors declare no conflict of interest.

#### References

- Maher, F.J. Wind loads on basic dome shapes. J. Struct. Div. 1965, 91, 219–228. [CrossRef]
- 2. Taniguchi, S.; Sakamoto, H.; Kiya, M.; Arie, M. Time-averaged aerodynamic forces acting on a hemisphere immersed in a turbulent boundary. *J. Wind Eng. Ind. Aerod.* **1982**, *9*, 257–273. [CrossRef]
- 3. Taylor, T.J. Wind pressures on a hemispherical dome. J. Wind Eng. Ind. Aerod. 1992, 40, 199–213. [CrossRef]
- 4. Ogawa, T.; Nakayama, M.; Murayama, S.; Sasaki, Y. Characteristics of wind pressures on basic structures with curved surfaces and their response in turbulent flow. *J. Wind Eng. Ind. Aerod.* **1991**, *38*, 427–438. [CrossRef]
- Savory, E.; Toy, N. Hemisphere and hemisphere-cylinders in turbulent boundary layers. J. Wind Eng. Ind. Aerod. 1986, 23, 345–364.
   [CrossRef]
- 6. Letchford, C.W.; Sarkar, P.P. Mean and fluctuating wind loads on rough and smooth parabolic domes. *J. Wind Eng. Ind. Aerod.* **2000**, *88*, 101–117. [CrossRef]

Sustainability **2023**, 15, 4635 21 of 22

7. Cheng, C.M.; Fu, C.L. Characteristic of wind loads on a hemispherical dome in smooth flow and turbulent boundary layer flow. *J. Wind Eng. Ind. Aerod.* **2010**, *98*, 328–344. [CrossRef]

- 8. Chevula, S.; Sanz-Andres, A.; Franchini, S. Aerodynamic external pressure loads on a semi-circular bluff body under wind gusts. *J. Fluid Struct.* **2015**, *54*, 947–957. [CrossRef]
- 9. Kim, Y.C.; Yoon, S.W.; Cheon, D.J.; Song, J.Y. Characteristics of wind pressures on retractable dome roofs and external peak pressure coefficients for cladding design. *J. Wind Eng. Ind. Aerod.* **2019**, *188*, 294–307. [CrossRef]
- 10. Lee, J.H.; Kim, Y.C.; Cheon, D.J.; Yoon, S.W. Wind pressure characteristics of elliptical retractable dome roofs. *J. Asian Archit. Build.* **2022**, *21*, 1561–1577. [CrossRef]
- 11. Tavakol, M.M.; Yaghoubi, M.; Ahmadi, G. Experimental and numerical analysis of airflow around a building model with an array of domes. *J. Build. Eng.* **2021**, *34*, 101901. [CrossRef]
- 12. Murakami, S. Overview of turbulence models applied in CWE-1997. J. Wind Eng. Ind. Aerod. 1998, 74-76, 1-24. [CrossRef]
- 13. Smagorinsky, J. General circulation experiments with the primitive equations: I. The basic experiment. *Mon. Weather Rev.* **1963**, 91, 99–164. [CrossRef]
- 14. Nicoud, F.; Ducros, F. Subgrid-scale stress modelling based on the square of the velocity gradient tensor. *Flow Turbul. Combust.* **1999**, *62*, 183–200. [CrossRef]
- 15. Germano, M.; Piomelli, U.; Moin, P.; Cabot, W.H. A dynamic subgrid-scale eddy viscosity model. *Phys. Fluids A-Fluid* **1991**, 3, 1760. [CrossRef]
- 16. Lilly, D.K. A proposed modification of the Germano subgrid-scale closure method. *Phys. Fluids A-Fluid* **1992**, 4, 633–635. [CrossRef]
- 17. Spalart, P.; Allmaras, S. A one-equation turbulence model for aerodynamic flows. Rech. Aerospatiale 1994, 1, 5–21. [CrossRef]
- 18. Launder, B.E.; Spalding, D.B. Lectures in Mathematical Models of Turbulence; Academic Press: London, UK, 1972.
- 19. Wilcox, D.C. Turbulence Modeling for CFD; DCW Industries: La Canada Flintridge, CA, USA, 1998.
- 20. Shih, T.H.; Liou, W.W.; Shabbir, A.; Yang, Z.; Zhu, J. A new k-ε eddy viscosity model for high reynolds number turbulent flows. *Comput. Fluids* **1995**, 24, 227–338. [CrossRef]
- 21. Yakhot, V.S.; Orszag, S.A.; Thangam, S.; Gatski, T.B.; Speziale, C.G. Development of turbulence models for shear flows by a double expansion technique. *Phys. Fluids A-Fluid* **1992**, *4*, 1510. [CrossRef]
- 22. Menter, F.R. Two-equation eddy-viscosity turbulence models for engineering applications. AIAA J. 1994, 32, 1598–1605. [CrossRef]
- 23. Menter, F.R. Eddy viscosity transport equations and their relation to the k-ε model. J. Fluid Eng. 1997, 119, 876–884. [CrossRef]
- 24. Menter, F.R.; Kuntz, M.; Langtry, R. Ten years of industrial experience with the SST turbulence model. *Turbul. Heat Mass Transf.* **2003**, *4*, 625–632.
- 25. Tavakol, M.M.; Yaghoubi, M.; Motlagh, M.M. Air flow aerodynamic on a wall-mounted hemisphere for various turbulent boundary layers. *Exp. Therm. Fluid Sci.* **2010**, *34*, 538–553. [CrossRef]
- 26. Tavakol, M.M.; Abouali, O.; Yaghoubi, M. Large eddy simulation of turbulent flow around a wall mounted hemisphere. *Appl. Math Model* **2015**, *39*, 3596–3618. [CrossRef]
- 27. Fu, C.L.; Cheng, C.M.; Lo, Y.L.; Cheng, D.Q. LES simulation of hemispherical dome's aerodynamic characteristics in smooth and turbulence boundary layer flows. *J. Wind Eng. Ind. Aerod.* **2015**, *144*, 53–61. [CrossRef]
- 28. Wood, J.N.; De Nayer, G.; Schmidt, S.; Breuer, M. Experimental investigation and large-eddy simulation of the turbulent flow past a smooth and rigid hemisphere. *Flow Turbul. Combust.* **2016**, 97, 79–119. [CrossRef]
- 29. Sadeghi, H.; Heristchian, M.; Aziminejad, A.; Nooshin, H. Wind effect on grooved and scallop domes. *Eng. Struct.* **2017**, *148*, 436–450. [CrossRef]
- 30. Fouad, N.S.; Mahmoud, G.H.; Nasr, N.E. Comparative study of international codes wind loads and CFD results for low rise buildings. *Alex. Eng. J.* **2018**, *57*, 3623–3639. [CrossRef]
- 31. Khosrowjerdi, S.; Sarkardeh, H.; Kioumarsi, M. Effect of wind load on different heritage dome buildings. *Eur. Phys. J. Plus* **2021**, 136, 1180. [CrossRef]
- 32. Franke, J.; Hirsch, C.; Jensen, A.G.; Krüs, H.W.; Schatzmann, M.; Westbury, P.S.; Miles, S.D.; Wisse, J.A.; Wright, N.G. Recommendations on the use of CFD in predicting pedestrian wind environment. In *COST Action C14 "Impact of Wind and Storms on City Life and Built Environment"*; Von Karman Institute: Rhode-Saint-Genese, Belgium, 2004.
- 33. Murakami, S. Setting the scene: CFD and symposium overview. Wind Struct. 2002, 5, 83–88. [CrossRef]
- 34. Tominaga, Y.; Stathopoulos, T. Numerical simulation of dispersion around an isolated cubic building: Model evaluation of RANS and LES. *Build. Environ.* **2010**, *45*, 2231–2239. [CrossRef]
- 35. American Society of Civil Engineers. *Minimum Design Loads and Associated Criteria for Buildings and Other Structures*; ASCE/SEI 7–16; American Society of Civil Engineers: Reston, VA, USA, 2016. [CrossRef]
- 36. Simiu, E.; Scanlan, R.H. Wind Effects on Structures: Fundamentals and Applications to Design, 3rd ed.; John Wiley and Sons, Inc.: New York, NY, USA, 1986.
- 37. Kaimal, J.C.; Finigan, J.J. Atmospheric Boundary Layer Flows: Their Structure and Measurement; Oxford University Press: Oxford, UK. 1994
- 38. Pope, S.B. Turbulent Flows; Cambridge University Press: Cambridge, UK, 2000; pp. 182–263.
- 39. Blocken, B. Computational Fluid Dynamics for urban physics: Importance, scales, possibilities, limitations and ten tips and tricks towards accurate and reliable simulations. *Build. Environ.* **2015**, *91*, 219–245. [CrossRef]

Sustainability **2023**, 15, 4635 22 of 22

40. Franke, J.; Hellsten, A.; Schlünzen, H.; Carissimo, B. Best practice guideline for the CFD simulation of flows in the urban environment. In Proceedings of the 11th Conference on Harmonisation within Atmospheric Dispersion Modelling for Regulatory Purposes, Cambridge, UK, 2–5 July 2007.

- 41. Savory, E.; Toy, N. The separated shear layers associated with hemispherical bodies in turbulent boundary layers. *J. Wind Eng. Ind. Aerod.* **1988**, *28*, 291–300. [CrossRef]
- 42. Hunt, J.C.; Wray, A.A.; Moin, P. Eddies, streams, and convergence zones in turbulent flows. In Proceedings of the 1988 Summer Program. Center for Turbulence Research, Buffalo, NY, USA, 20–22 November 1988.

**Disclaimer/Publisher's Note:** The statements, opinions and data contained in all publications are solely those of the individual author(s) and contributor(s) and not of MDPI and/or the editor(s). MDPI and/or the editor(s) disclaim responsibility for any injury to people or property resulting from any ideas, methods, instructions or products referred to in the content.